Supplementary Information for:

Graph Neural Network based elastic deformation emulators for magmatic reservoirs of complex geometries

Taiyi A. Wang[1,2], **Ian W. McBrearty**[1], **Paul Segall**[1]

[1]Department of Geophysics, Stanford University
[2]Now at Seismological Laboratory, California Institute of Technology

Contents of this file

1 Dislocation boundary element model

The surface deformation data sets used to train the Graph Neural Network Emulators are computed using a customized boundary element code based on triangular dislocation solutions (Nikkhoo & Walter, 2015), which we describe in details here. The goal is to solve for the surface displacement due to pressurization/depressurization of a 3D magma reservoir in a homogeneous, isotropic, linear elastic half space. The magma reservoir is represented as a cavity, the walls of which are subjected to traction changes due to pressure change in magma. Solutions of the displacement field thus satisfy the following equations,

$$\partial_j \sigma_{ij} = 0, \tag{1}$$

$$\sigma_{ij} = 2\mu\epsilon_{ij} + \lambda\epsilon_{kk}\delta_{ij}, \tag{2}$$

$$T_i\Big|_{z=0} = [0,0,0]^T, \tag{3}$$

$$T_i n_i\Big|_{\mathcal{S}} = -\Delta p, \tag{4}$$

where indices $i, j = x, y, z$ and repeated indices indicate summation. σ_{ij}, ϵ_{ij}, and $T_i = \sigma_{ij} n_j$ are the perturbation stress tensor, strain tensor, and traction changes relative to an equilibriated background state. n_j is the normal vector relative to surfaces (upward for the free surface and outward for cavity walls). Eqn. 1 and 2 are the static equilibrium equation and the Hooke's law for isotropic material (μ: shear modulus, λ: Lamé constant), respectively. Eqn. 3 describes the traction-free boundary condition at the surface. Eqn. 4 describes the spatially uniform normal traction change (following tension positive convention) at the boundary of the cavity, $\mathcal{S}$, induced by pressure change in magma, Δp. Additionally, all shear tractions on $\mathcal{S}$ vanish.

We first tessellate $\mathcal{S}$ with N triangular elements, and solve for the dislocation (relative motion across an element) at each triangular element. Denoting the perturbation traction at the p th element as T_i^p and the dislocation at the q th element as δ_i^q, the two quantities are related by the stiffness matrix, S_{ij}^{pq},

$$T_i^p = S_{ij}^{pq}\delta_j^q, \tag{5}$$

Corresponding author: Taiyi Wang, taiyi@caltech.edu

where $p, q = 1, 2, ..., N$. S_{ij}^{pq} relates dislocation in direction j at element q with traction changes in direction i at element p, and is computed using dislocation boundary element solutions (Nikkhoo & Walter, 2015).

In practice, it is desirable to work with dislocation and traction changes in coordinate systems local to each element, given the non-Euclidean geometry of magma reservoirs. Here we denote the two orthogonal directions co-plane with the triangular element as ϕ and θ, and the direction normal to the element as r. Because Eqn. 1, 2, 3 are automatically satisfied by the dislocation solutions, we next apply the boundary condition on the cavity surface (Eqn. 4) in local coordinates and invert the traction-dislocation relationship (Eqn. 5), obtaining dislocations at each element, q,

$$\delta_j^q = \{S_{ij}^{pq}\}^{-1} T_i^p, \tag{6}$$

where $i, j = \phi, \theta, r$ and $T_i^p = [0, 0, -\Delta p]^T$. Displacements on the surface are then computed using the half-space Green's functions relating dislocation with displacements (Nikkhoo & Walter, 2015).

2 Bayesian Markov Chain Monte Carlo inversion

We employ a Bayesian framework to estimate the probability density functions (PDFs) of model parameters (reservoir geometry, location, volume, pressure change). The Bayes' theorem states

$$P(\boldsymbol{m}|\boldsymbol{d}) \propto P(\boldsymbol{d}|\boldsymbol{m})P(\boldsymbol{m}), \tag{7}$$

where $\boldsymbol{m}$ denotes model parameters and $\boldsymbol{d}$ the data. Thus the probability of a model conditioned on data, $P(\boldsymbol{m}|\boldsymbol{d})$ (i. e. the posterior), is proportional to the product between the probability of the data conditioned on the model $P(\boldsymbol{d}|\boldsymbol{m})$ (i.e. the likelihood) and the probability of the model parameters independent of the data, $P(\boldsymbol{m})$ (i.e. the prior).

We employ uniform prior distributions for parameters in all inversions in this study. For the inversion with synthetic deformation associated with a spheroidal reservoir (Fig. 5 in the main text), we use the following bounds on the parameters: $V = [1, 100]$ km^3, $\alpha \in [1, 10]$, $\Delta x \in [-10, 10]$ km, $\Delta y \in [-10, 10]$ km, $\Delta z \in [-20, -1]$ km, $\theta_x \in [0, \pi/2]$, $\theta_z \in [0, 2\pi]$. $\Delta p/\mu$ is fixed at 10^{-3}. For the inversion with synthetic deformation associated with the reservoir with a north-south trending ridge on the top (Fig. 6 in the main text), we use the following bounds on the parameters: $\Delta x \in [-10, 10]$ km, $\Delta y \in [-10, 10]$ km, $\Delta z \in [-100, -1]$ km, $R_{max} \in [0.316, 10]$ km, $c_0^0 \in [0, 20]$, $\mathrm{Re}(\{c_l^m\}_{0 \le l \le 5}) \in [-1, 1]$, and $\mathrm{Im}(\{c_l^m\}_{0 \le l \le 5}) \in [-1, 1]$. $\Delta p/\mu$ is fixed at 10^{-3}. All parameter bounds are the same for the reservoir with a threefold axisymmetry on the top (Fig. 7 in the main text), except that $\Delta z \in [-10, -1]$ km.

We estimate the likelihood using the affine-invariant Markov Chain Monte Carlo (MCMC) ensemble sampler (Foreman-Mackey et al., 2013). We assume that the observation errors are normally distributed, such that,

$$P(\boldsymbol{d}|\boldsymbol{m}) = (2\pi)^{-M/2} \det(\boldsymbol{C})^{-1/2} \times \exp[-\frac{1}{2}(\boldsymbol{d} - \boldsymbol{G}(\boldsymbol{m}))^T \boldsymbol{C}^{-1} (\boldsymbol{d} - \boldsymbol{G}(\boldsymbol{m}))]. \tag{8}$$

Here, M is the total number of data points, $\boldsymbol{C}$ the data covariance matrix, $\boldsymbol{G}$ is the forward model operator (i. e. the emulators).

The accuracy of Eqn. 8 is predicated on having the correct covariance matrices for each data set. By definition, the synthetic data do not have observation error, so we assume that $\boldsymbol{C}$ is a diagonal matrix, with each diagonal entry being identically $\sigma = 2 \times 10^{-3}$ m. This value is chosen by trial and error to ensure the convergence of the Markov Chain in reasonable time, because $\boldsymbol{C}$ controls the magnitude of $P(\boldsymbol{d}|\boldsymbol{m})$.

Example No.	Δz **(km)**	θ_x (°)	θ_z (°)	R_a **(km)**	R_b **(km)**
1[1]	-7.29	32.0	27.8	5.81	1.16
2 [2]	-6.09	84.0	59.1	0.219	0.730
3 [1]	-5.37	16.8	87.9	0.917	0.917
4 [1]	-19.5	87.4	74.0	18.5	9.24

[1] In the training data set.
[2] In the validation data set.

Table 1: Parameters for example predictions of the spheroid emulator. $\Delta p/\mu = 10^{-3}$, $\Delta x = 0$, $\Delta y = 0$.

Example No.	Δz **(km)**	R_{max} **(km)**	c_l^0	c_l^1	c_l^2	c_l^3	c_l^4	c_l^5
1[1]	-11.3	7.73	1.75					
			-0.26	$1.67 - 0.397i$				
			2.53	$0.764 + 0.151i$	$-0.953 - 0.0317i$			
			0.270	$0.782 + 0.128i$	$0.119 - 0.855i$	$-0.0801 - 0.0541i$		
			0.00967	$0.259 + 0.0190i$	$-0.0346 + 0.112i$	$-0.0851 + 0.139i$	$0.00864 + 0.481i$	
			0.182	$-0.0489 + 0.857i$	$0.386 + 0.126i$	$-0.108 - 0.243i$	$-0.478 - 0.759i$	$0.945 - 0.0867i$
2 [3]	-2	1	4					
			0	0				
			0	0	0			
			0	0	0	0		
			0	0	0	1	0	
			0	0	0	0	0	0
3[1]	-2.36	0.765	13.2					
			-0.246	$-0.519 + 0.629i$				
			0.0467	$-0.585 - 0.606i$	$0.228 - 0.758i$			
			0.901	$-0.00655 - 0.516i$	$0.803 - 0.276i$	$-0.0570 - 0.0491i$		
			-0.742	$-0.0225 - 0.00274i$	$-0.140 + 0.401i$	$-0.661 + 0.683i$	$-0.770 - 0.605i$	
			-0.216	$0.0947 + 0.447i$	$-0.339 + 0.396i$	$0.0930 + 0.138i$	$-0.688 - 0.164i$	$-0.0342 + 0.0629i$

[1] In the training data set.
[2] In the validation data set.
[3] Randomly chosen model not in training or validation data set.

Table 2: Parameters for example predictions of the general shape emulator. Each row corresponds to a spherical harmonics degree, l, from 0 to 5. $\Delta p/\mu = 10^{-3}$, $\Delta x = 0$, $\Delta y = 0$ (Continued).

Example No.	Δz **(km)**	R_{max} **(km)**	c_l^0	c_l^1	c_l^2	c_l^3	c_l^4	c_l^5
4[1]	-5.44	0.944	1.55					
			0.00403	$0.0321 + 0.0000362i$				
			0.168	$0.125 + 0.232i$	$-0.0852 + 0.0902i$			
			-0.000548	$0.0110 + 0.0000162i$	$0.00363 + 0.0000944i$	$0.0275 + 0.0000916i$		
			-0.0633	$0.0267 + 0.0496i$	$-0.0567 + 0.0703i$	$-0.0492 - 0.00206i$	$-0.0315 - 0.0117i$	
			-0.000607	$0.00505 - 0.000000297i$	$0.00167 + 0.0000420i$	$0.0141 + 0.0000663i$	$0.00290 + 0.000155i$	$0.0240 + 0.000132i$
5[2]	-3.86	2.99	1.00					
			-0.0193	$0.0757 + 0.000175i$				
			-0.0179	$-0.287 - 0.134i$	$0.231 + 0.0903i$			
			0.118	$-0.0206 - 0.0083i$	$-0.0202 + 0.0252i$	$0.0469 - 0.0440i$		
			-0.00770	$0.0660 - 0.000485i$	$-0.0169 + 0.000166i$	$-0.0650 + 0.00155i$	$0.0411 - 0.00201i$	
			-0.00559	$0.000348 + 0.00000148i$	$0.00640 - 0.0000139i$	$0.00763 + 0.000000677i$	$-0.0146 + 0.0000402i$	$0.0350 - 0.0000581i$

[1] In the training data set.
[2] In the validation data set.

Table 2: Parameters for example predictions of the general shape emulator. Each row corresponds to a spherical harmonics degree, l, from 0 to 5. $\Delta p/\mu = 10^{-3}$, $\Delta x = 0$, $\Delta y = 0$.

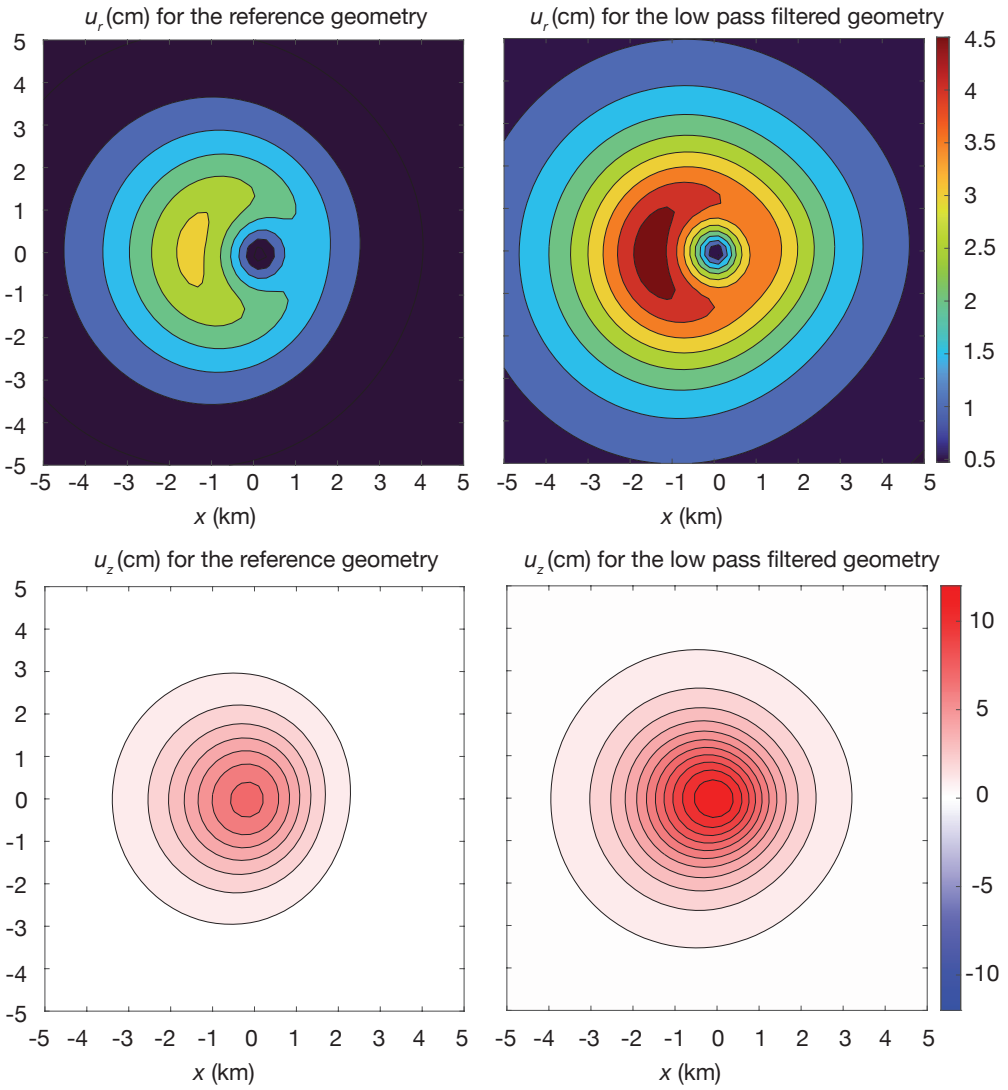

Figure S1: Comparison of surface deformation for the hypothetical, reference reservoir geometry and the low-pass filtered reservoir geometry (done via filtering of spherical harmonic modes) shown in Fig. 1 of the main text. Displacements are calculated using the boundary element method. The low-pass filtered reservoir geometry produces the same displacement pattern as that of the reference geometry, but a higher displacement amplitude, because low pass filtering inevitably leads to a more spherical reservoir geometry with larger volume. u_r, u_z: radial and vertical displacement, respectively. Calculations assume $\Delta p/\mu = 10^{-3}$.

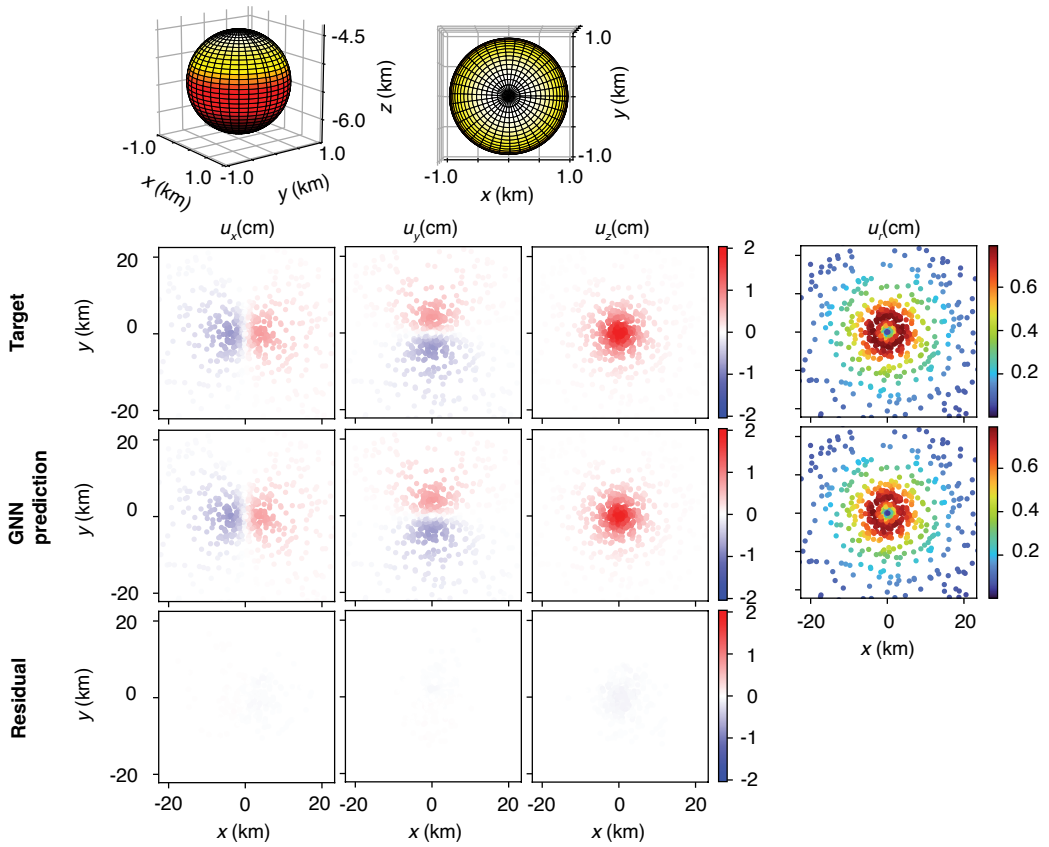

Figure S2: Spheroid emulator prediction vs. BEM prediction. Example 3.

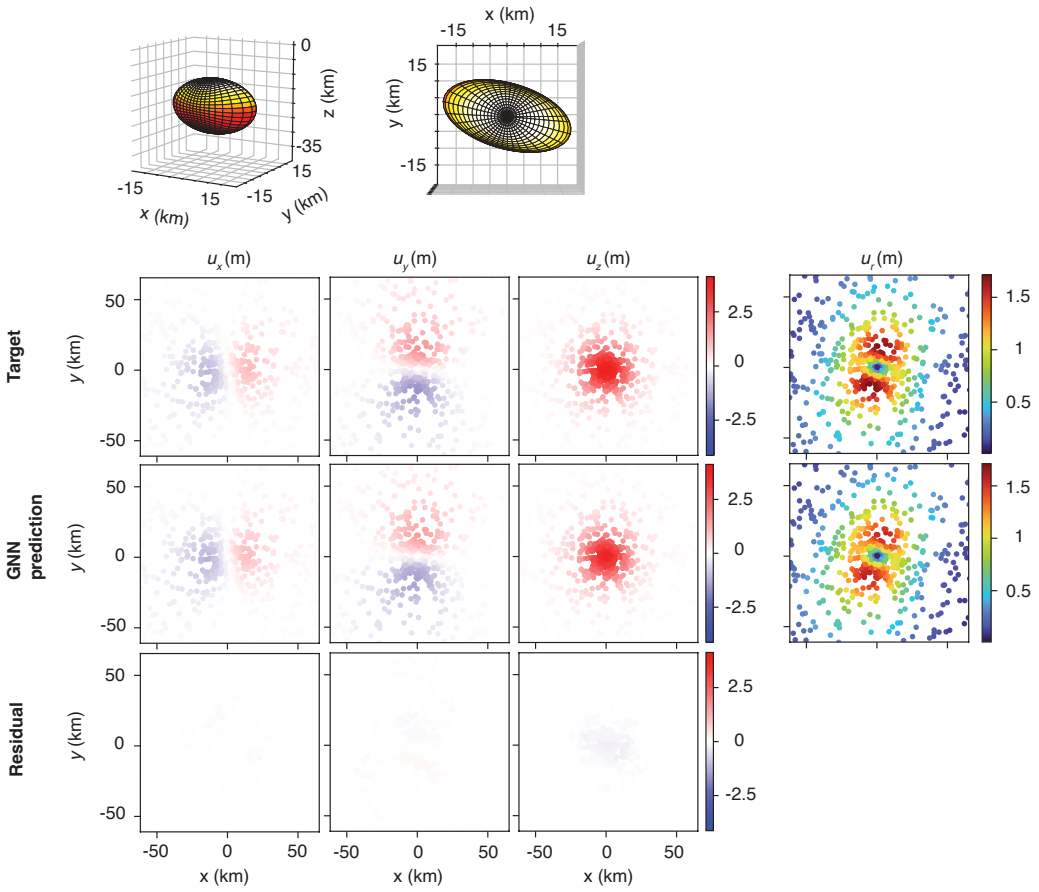

Figure S3: Spheroid emulator prediction vs. BEM prediction. Example 4.

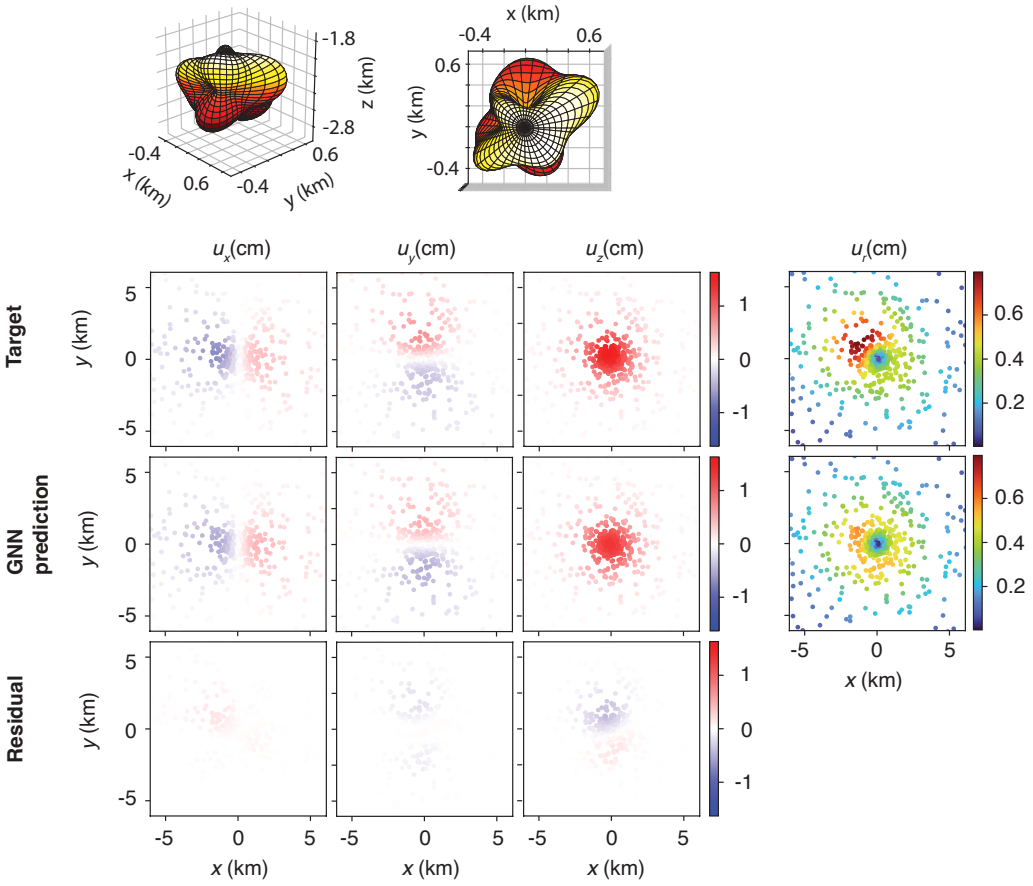

Figure S4: General shape emulator prediction vs. BEM prediction. Example 3.

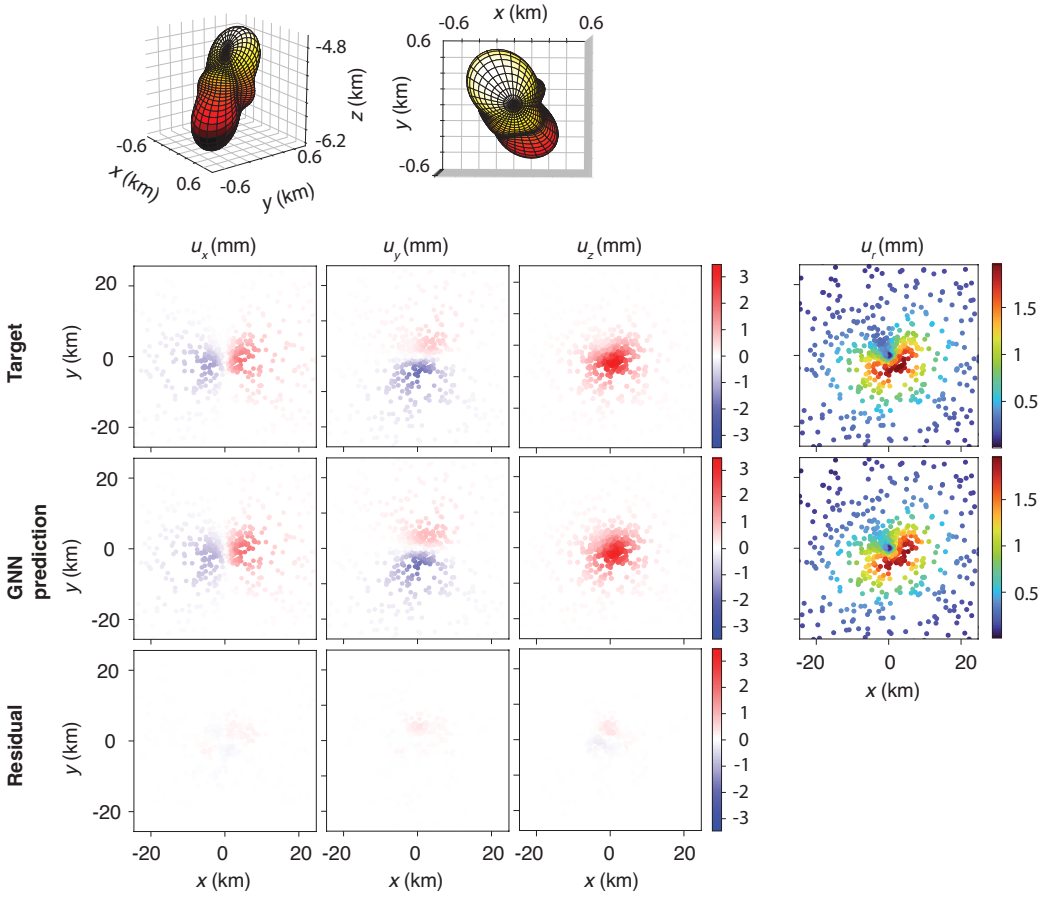

Figure S5: General shape emulator prediction vs. BEM prediction. Example 4.

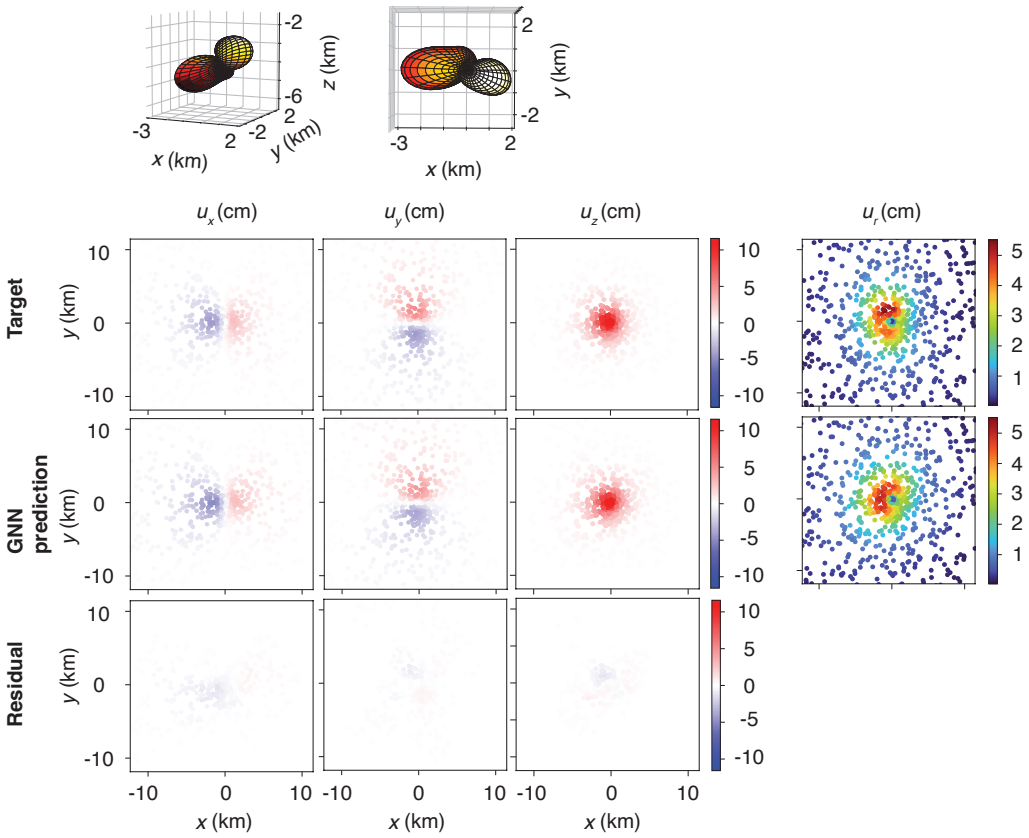

Figure S6: General shape emulator prediction vs. BEM prediction. Example 5.

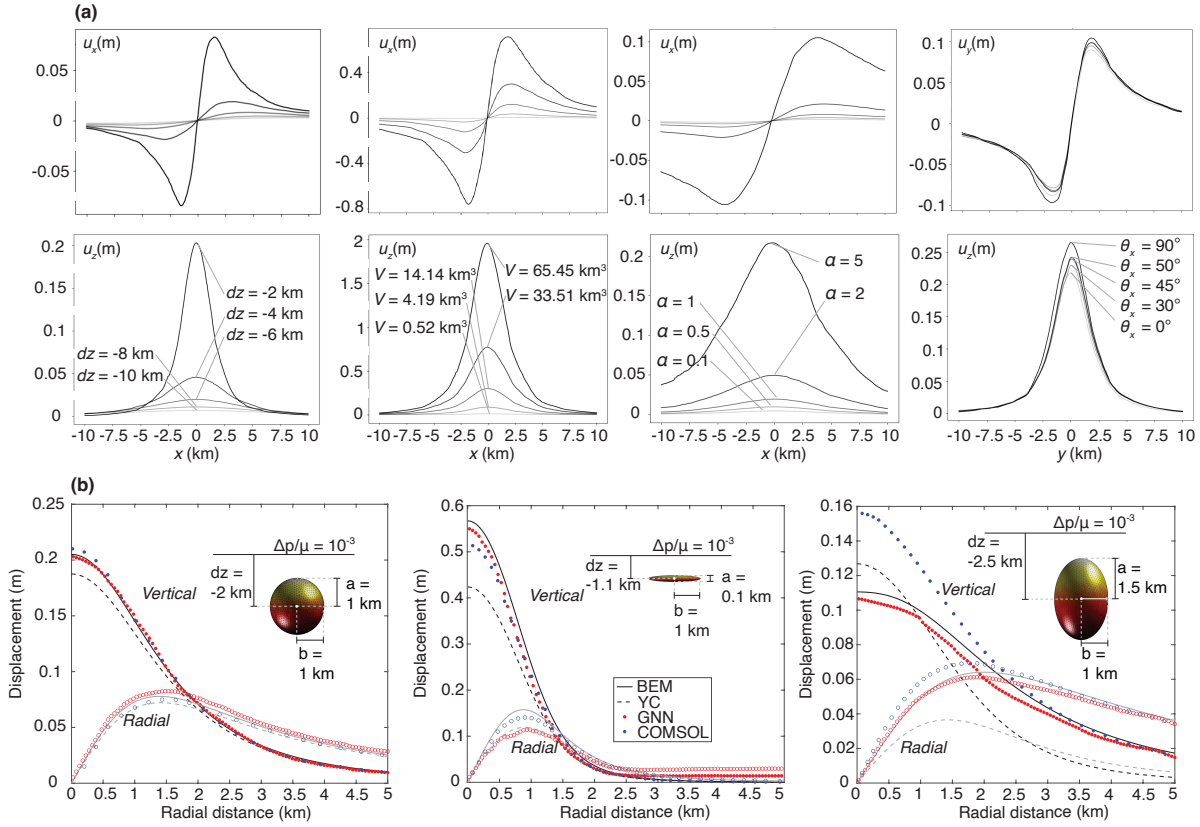

Figure S7: Verifying surface displacement predictions of the spheroid emulator. (a) Sensitivity of emulator-predicted surface displacement to reservoir centroid depth, Δz, reservoir volume, V, reservoir aspect ratio, α, and rotation angle relative to the x-axis, θ_x. The default parameters are: $\Delta x = 0$ km, $\Delta y = 0$ km, $\Delta z = -3$ km, $V = 4.2$ km^3, $\alpha = 1$, $\theta_x = \theta_z = 0°$. Assuming $\Delta z = -6$ km when testing variations in α. Assuming $\alpha = 1.5$ and $\Delta z = -2.5$ km when testing variations in θ_x. (b) Comparing emulator predictions with BEM solutions, Yang-Cervelli (YC) semi-analytical solutions (Cervelli, 2013), and COMSOL finite element solutions for a sphere ($\alpha = 1$), an oblate spheroid ($\alpha = 0.1$), and a prolate spheroid ($\alpha = 1.5$).

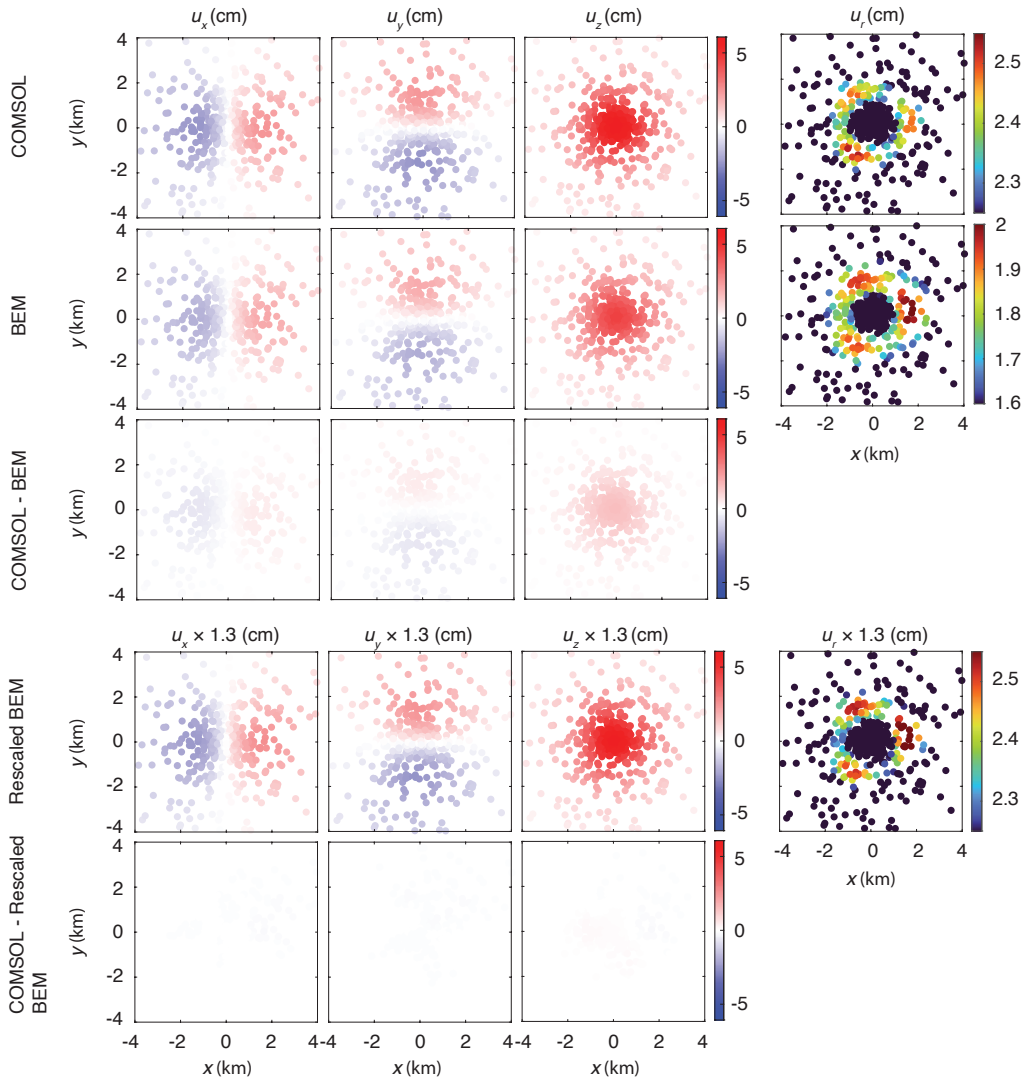

Figure S8: Verifying the boundary element method for complex reservoir geometries. For reservoir geometries with high spatial frequencies, BEM error tends to be non-negligible. In the case of the reservoir geometry with a threefold axisymmetry with regard to z, such as shown in Fig. 3d of the the main text, the BEM error manifests as a scaling factor in the amplitude of the displacement field.

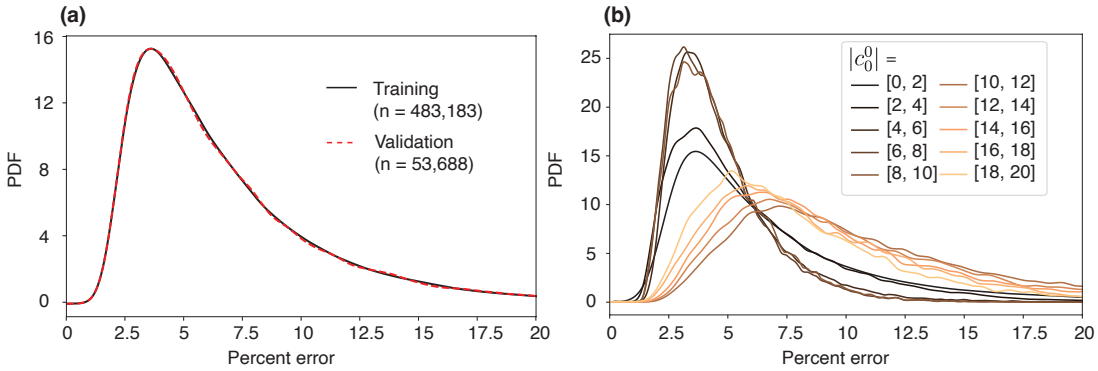

Figure S9: (a) Distribution of 90th percentile relative error for each realization of complex reservoir geometry, for training versus validation data sets. Relative error is defined by Eqn. 10 in the main text. (b) Distribution of 90th percentile relative error for each realization of complex reservoir geometry, plotted as a function of the magnitude of the lowest mode of spherical harmonics, c_0^0.

References

Cervelli, P. F. (2013). Analytical expressions for deformation from an arbitrarily oriented spheroid in a half-space. In *AGU Fall Meeting Abstracts* (Vol. 2013, pp. V44C–06).

Foreman-Mackey, D., Hogg, D. W., Lang, D., & Goodman, J. (2013). emcee: The MCMC hammer. *Publications of the Astronomical Society of the Pacific*, *125*(925), 306.

Nikkhoo, M., & Walter, T. R. (2015). Triangular dislocation: an analytical, artefact-free solution. *Geophysical Journal International*, *201*(2), 1119–1141.